https://doi.org/10.5194/egusphere-2026-1181
Preprint. Discussion started: 7 April 2026

Distinguishing run-up height from pressure distribution during avalanche impact on narrow obstacles: mechanisms and semi-empirical prediction

Michael J. Kohler[1,2], Johan Gaume[1,3], Christophe Ancey[2], and Betty Sovilla[1]

[1]WSL Institute for Snow and Avalanche Research SLF, Flueelastrasse 11, 7260 Davos Dorf, Switzerland
[2]EPFL Environmental Hydraulics Laboratory, Station 18, 1015 Lausanne, Switzerland
[3]ETH Zurich Chair of Alpine Mass Movements, Stefano-Franscini-Platz 5, 8093 Zurich, Switzerland

Correspondence: Michael J. Kohler (michael.kohler@slf.ch)

Abstract. In current engineering practice, run-up height is assumed to define the vertical extent of significant impact pressure of snow avalanches on narrow obstacles, such as cableway masts or transmission towers. Laboratory experiments indicate that this assumption is invalid in fast, inertia-driven regimes; however, the underlying mechanisms remain poorly understood, limiting the physical basis for improving design practice. To clarify these mechanisms and refine engineering formulations, we conduct a comprehensive numerical investigation using a three-dimensional Material Point Method, varying avalanche velocity and rheological parameters. Our results substantiate that run-up height and the vertical extent of significant impact pressure, which we term *pressure height*, are distinct quantities governed by different mechanisms. Both include a gravity-driven component controlled by avalanche rheology, largely independent of flow velocity. In fast flows, however, the two quantities diverge: run-up height gains a dominant inertia-driven component scaling with the square of flow velocity, with avalanche rheology controlling energy dissipation. Pressure height, by contrast, remains velocity-independent. This divergence arises from flow deflection at a granular dead zone near the obstacle base, where momentum is redirected, and impact pressure concentrates. Building on these distinctions, we propose separate semi-empirical formulations for run-up height and pressure height. The run-up formulation follows the structure of the widely used Swiss avalanche guidelines, but replaces simplified avalanche-type classifications with a rheological parametrization. The pressure-height relation adopts the same framework, while reflecting its distinct, velocity-independent governing mechanism.

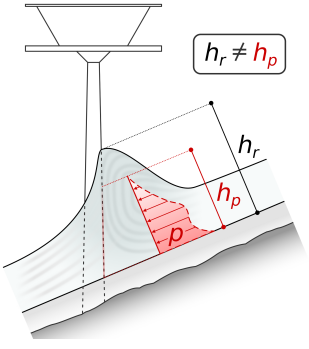

Graphical abstract (adapted from Margreth et al., 2015)

https://doi.org/10.5194/egusphere-2026-1181
Preprint. Discussion started: 7 April 2026

1 Introduction

Natural granular flows such as snow avalanches are major natural hazards in mountainous regions, causing loss of life and substantial damage to infrastructure (Techel et al., 2016; Ortner et al., 2023). Assessing their destructive power is a central component of hazard mitigation, and it requires understanding the physical processes that govern impact. A key process is run-up: the upward rise of material along the upstream face of an obstacle as the flow decelerates and transfers momentum to the structure (Iverson et al., 2016). Run-up height is a central engineering quantity across a broad range of structures. For wide obstacles such as avalanche dams, it determines crest elevation and retention capacity (Jóhannesson et al., 2009). For narrow obstacles such as cableway masts or transmission towers, which are often located in remote and exposed terrain (Vallero et al., 2026), it governs the risk of damage to protruding elements that may be struck by upward-moving material, and is commonly assumed to define the vertical extent of idealized impact pressure distributions (Rudolf-Miklau et al., 2014; Margreth et al., 2015). The wide–narrow distinction, classically defined by an obstacle width of approximately three times the flow height, or $2\,\mathrm{m}$, according to the Swiss avalanche guidelines (Margreth et al., 2015), has important implications for the mechanical description of the problem. For wide obstacles, the impact problem can be approximated under plane-strain conditions, enabling a quasi-two-dimensional analytical description (e.g., Mcclung and Mears, 1995; Hákonardóttir, 2003; Mejean et al., 2017; Faug, 2021). For narrow obstacles, however, the flow partially bypasses the structure laterally, making the impact problem inherently three-dimensional (Wu et al., 2023; Lin et al., 2025). This complicates the mechanical description and requires many restrictive assumptions in any analytical treatment (cf. Faug et al., 2010; Bartelt et al., 2018).

In the absence of generally accepted analytical solutions for narrow obstacles, engineering practice relies on empirical formulations calibrated against observations to predict run-up height (Salm et al., 1990). The most prominent approach is based on the velocity head from Bernoulli's principle

$$h_v = \frac{v^2}{2g}, \tag{1}$$

which describes the transformation of kinetic energy to potential energy upon impact. Therein, h_v denotes the velocity head expressed as an equivalent height, v is the flow velocity, and g is the gravitational acceleration. This concept was already used by Voellmy (1955) in his pioneering work on snow avalanche dynamics and has since been adopted in the widely used Swiss guidelines for snow avalanche engineering (Margreth et al., 2015). Within this framework, Eq. (1) is augmented by two empirical factors to account for the influence of obstacle width and energy dissipation (cf. Sect. 4, for the full equation). Avalanche rheology is only crudely reflected in the energy dissipation factor, without an explicit link to measurable material constants. Yet experimental observations show that flow rheology strongly influences the morphology of flow–obstacle interaction (Choi et al., 2015; Armanini et al., 2011), implying that the physical mechanisms governing run-up are poorly represented by this framework and that predictive reliability is limited.

The limitations extend beyond run-up height estimation itself. In laboratory experiments on supercritical granular flows impacting narrow obstacles, Hauksson et al. (2007) showed that the total impact force became independent of obstacle height once it exceeded approximately three flow heights, which is substantially below the corresponding run-up heights. This shows that run-up height does not reliably indicate the vertical extent of impact pressure in such configurations, as assumed in current

https://doi.org/10.5194/egusphere-2026-1181
Preprint. Discussion started: 7 April 2026

design practice. Sovilla et al. (2008b) further demonstrated that the Swiss guidelines formulation can produce physically inconsistent force predictions, providing additional evidence that the framework lacks a sound physical basis.

Addressing these inconsistencies requires capturing the transient three-dimensional impact process while explicitly accounting for avalanche rheology. Recent numerical studies of snow-avalanche impact on narrow obstacles could not resolve run-up formation due to computational constraints imposed by their discrete modeling approach (Kyburz et al., 2020, 2022). Continuum approaches based on the Material Point Method (MPM) are a computationally efficient alternative, capturing both transient run-up dynamics and avalanche rheology, as recently demonstrated for impact pressure analysis (Kohler et al., 2025). However, run-up formation and its relation to impact pressure distribution remain uninvestigated.

Here, we pursue two main objectives. Our first objective, addressed in Sect. 3, is to clarify the physics of run-up on vertical narrow obstacles. Specifically, we investigate how run-up height depends on bulk rheological parameters and how it relates to the vertical extent of significant impact pressure. Our second objective, addressed in Sect. 4, is to translate these insights into a practical framework. We propose a semi-empirical extension of the velocity head formulation that explicitly incorporates rheological parameters and introduce a new metric to better quantify the vertical extent of significant impact pressure within the Swiss guidelines framework.

Together, these objectives address a gap that has direct consequences for efficient structural design: the assumption that run-up height defines the vertical extent of significant impact pressure on narrow obstacles is not physically justified, and this paper provides both the mechanistic explanation and a practical alternative.

2 Methodology

2.1 Numerical framework

2.1.1 The Material point method (MPM)

MPM combines the advantages of particle-based and grid-based methods, making it ideal for large-deformation flows such as avalanches. In MPM, a body is discretized into Lagrangian material points (MPs) carrying all state variables, such as deformation or stress states. The MPs move through an Eulerian background grid used to compute spatial derivatives and solve the momentum balance and constitutive equations (Sulsky et al., 1994; Stomakhin et al., 2013). In each time step, quantities are transferred between MPs and grid nodes using mapping functions, and the grid is reset. This prevents mesh distortion issues, typical of methods employing Lagrangian meshes.

We employ the three-dimensional (3D) MPM framework of Gaume et al. (2018) using quadratic B-Spline mapping functions, which closely follows the explicit symplectic Euler scheme of Stomakhin et al. (2013). Further details can be found in the original publications, the references therein, and our previous work (Kohler et al., 2025). This framework, together with its constitutive model for snow, has been validated and used extensively in numerical avalanche dynamics (e.g., Li et al., 2021; Védrine et al., 2022).

https://doi.org/10.5194/egusphere-2026-1181
Preprint. Discussion started: 7 April 2026

2.1.2 Constitutive model

The avalanching material is modeled using the large-strain elasto-plastic law for snow of Gaume et al. (2018), built around a cohesive Modified Cam–Clay (cMCC) plasticity model (Roscoe and Burland, 1968). The macroscopic rheology is mainly controlled by three plasticity parameters: the internal friction M, a cohesion parameter β, and the plastic compressibility $\chi(p_c)$ (Li et al., 2024).

M and β can be combined into an effective internal friction (Ritter et al., 2020)

$$M' = \frac{\beta+1}{(1-\beta)\sqrt{2\beta+1}}M, \tag{2}$$

which can be interpreted as a proxy for the material's angle of repose (Willibald et al., 2020; Eidevåg et al., 2022). M' is related to the Coulomb friction angle φ' through $\varphi' = \arcsin\left(3M'/(M'+6)\right)$ (Ortiz and Pandolfi, 2004) (cf. Fig. 1). We use M' as a primary rheological descriptor throughout this study, as it captures the combined effect of friction and cohesion in a single physically interpretable parameter.

Both M and β appear in the cMCC yield function

$$y(p,q) = q^2(1+2\beta) + M^2\left(p+\beta p_c\right)\left(p-p_c\right), \tag{3}$$

expressed in terms of the mean (compressive) stress $p = -\operatorname{tr}(\boldsymbol{\tau})/3$, and the *Von Mises* equivalent stress $q = (3/2\boldsymbol{s}:\boldsymbol{s})^{1/2}$, where $\boldsymbol{s} = \boldsymbol{\tau} + p\boldsymbol{I}$ is the deviatoric part of the Kirchhoff stress tensor $\boldsymbol{\tau}$. The elastic behavior is described through a Saint-Venant–Kirchhoff law. The yield function forms a semi-elliptical curve in $p-q$ space (cf. Kohler et al., 2025), which is a common assumption for highly porous media such as snow, supported by microstructure-based studies (Ritter et al., 2020; Blatny et al., 2021). The pre-consolidation pressure p_c sets the size of the elastic domain: the vertices of the semi-ellipse along the p-axis lie at p_c in compression and at $p_t = -\beta p_c$ in hydrostatic tension, while M controls the vertex in the deviatoric direction and hence the shear strength. For plastic stress states, the plastic strain follows the associative flow rule proposed by Simo and Meschke (1993).

When the material gets compacted, p_c grows, and the yield surface expands according to the hardening law (Ortiz and Pandolfi, 2004)

$$p_c = K\sinh\left(\xi\max\left(-\varepsilon_V^P, 0\right)\right), \tag{4}$$

where K is the bulk modulus, ξ is a hardening parameter, and $\varepsilon_V^P = \log J_P$ is the plastic volumetric Hencky strain, with J_P the plastic Jacobian (cf. Kohler et al., 2025, for further details and definitions). Hardening depends solely on volumetric deformation. Compaction ($\dot{\varepsilon}_V^P < 0$) expands the yield surface, whereas dilation ($\dot{\varepsilon}_V^P > 0$) contracts it and causes softening. The hardening parameter ξ controls the rate of this evolution and therefore principally affects the material's plastic compressibility. To aid physical interpretation, we express compressibility through the parameter $\chi(p_c = 25)$, which can be interpreted as a plastic density-increase factor evaluated at a reference pre-consolidation pressure of $p_c = 25\,\mathrm{kPa}$ for a given ξ; the correspondence between ξ and $\chi(p_c = 25)$ is given in Table 1 and its derivation is given in Appendix A1.

https://doi.org/10.5194/egusphere-2026-1181
Preprint. Discussion started: 7 April 2026

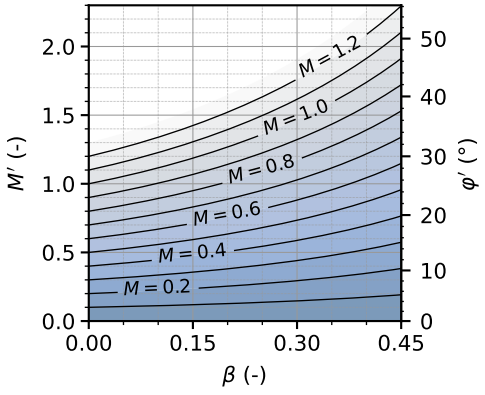

Figure 1. Effective internal friction M' and effective internal friction angle φ' over β for different values of M, calculated from Eq. (2)

Table 1. Fixed and varied material parameters of the avalanche

fixed material parameters:			
initial bulk density	ρ_0	($\mathrm{kg\,m^{-3}}$)	300
Young's modulus	E	(kPa)	1000
Poisson ratio	ν	(-)	0.1
bulk modulus[a]	K	(kPa)	416.67
initial pre-consolidation pressure	$p_{c,0}$	(kPa)	10
varied material parameters:			
CSL slope (friction)	M	(-)	$\{0.0, 0.4, 0.8, 1.2\}$
p_t/p_c (cohesion)	β	(-)	$\{0.0, 0.15, 0.3, 0.45\}$
plastic compressibility	$\chi(p_c = 25)$	(%)	$\{205.3, 127.1, 107.5, 102.4, 100.7, 100.2\}$[b]

[a] Follows from E and ν: $K = E/(3(1-2\nu))$.

[b] This corresponds to the hardening parameters $\xi = 0.05, 0.15, 0.5, 1.5, 5$, and 15, respectively. For snow-avalanches at the density used here, the relevant parameter range is $\chi(p_c = 25) \in \{107.5,\ 102.4,\ 100.7\}\%$ (i.e., $\xi \in \{0.5,\ 1.5,\ 5\}$). Accordingly, we restrict our semi-empirical model fitting to this range.

https://doi.org/10.5194/egusphere-2026-1181
Preprint. Discussion started: 7 April 2026

2.2 Numerical setup

We adopt the conveyor-belt setup of Kohler et al. (2025), in which the avalanche travels horizontally and impacts a rigid, vertical, rectangular obstacle. The avalanche is driven at a prescribed velocity rather than released from a chute, providing precise control of the flow velocity. The resulting motion resembles a plug flow, which can be seen as an idealization of a sheared avalanche in which we ignore the velocity profile and focus on the average velocity.

The initial flow height H and the obstacle width w are fixed at $H = w = 1.75\,\mathrm{m}$. We simulate a confined strip of the avalanche rather than the full width to limit computational cost, with the domain width W chosen sufficiently large to minimize boundary effects and adjusted based on the compressibility (cf. Fig. 2). The computational grid spacing is $dx = 0.25\,\mathrm{m}$. Flow velocity is maintained by frictional sidewalls, while the bottom boundary is frictionless. A schematic of the numerical setup listing all geometrical properties is shown in Fig. 2.

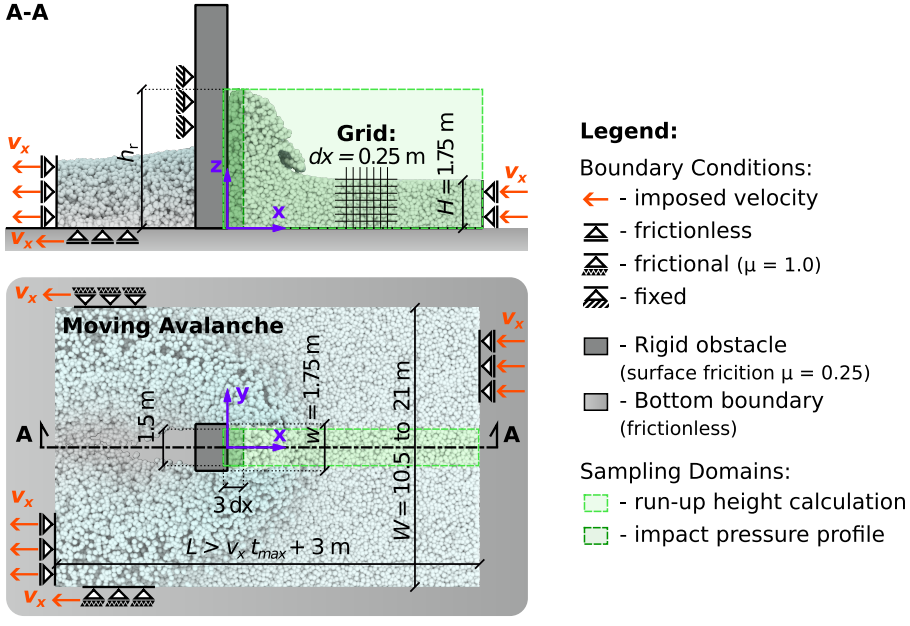

Figure 2. Schematic of the numerical setup adopted and adapted from Kohler et al. (2025), illustrating the dimensions and boundary conditions. The upper panel shows a longitudinal section, while the lower panel provides a top-down view. W follows from $W = (6 + 3\log(\xi/0.05))w$, with w the obstacle width

The flow parameter ranges in Table 2 are selected to cover typical snow-avalanche regimes (Köhler et al., 2018; Sovilla et al., 2008a). For impact scenarios, flow regimes can be characterized by the Froude number $\mathrm{Fr} = v/\sqrt{gH}$, where v is the flow velocity, g is gravitational acceleration, and H is the flow height. Fr expresses the ratio of inertial to gravitational forces: subcritical flows ($\mathrm{Fr} < 1$) are gravity-driven, supercritical flows ($\mathrm{Fr} > 1$) are inertia-driven, and the range $0.3 < \mathrm{Fr} < 3$ is sometimes referred to as transitional (Faug, 2015; Kohler et al., 2025). Real snow avalanches span a wide range, from slow, dense flows below $\mathrm{Fr} = 1$ to fast mixed powder snow avalanches beyond $\mathrm{Fr} = 7$ (Köhler et al., 2018).

https://doi.org/10.5194/egusphere-2026-1181
Preprint. Discussion started: 7 April 2026

The material parameter ranges in Table 1 are selected based on previous MPM snow-modeling studies (e.g., Li et al., 2020, 2021; Kyburz et al., 2024). The elasticity parameters E and ν, the initial pre-consolidation pressure $p_{c,0}$, and the initial bulk density ($\rho_0 = 300\,\mathrm{kg\,m^{-3}}$, a common estimate in avalanche engineering) are kept fixed. For each Fr, we perform at least 48 simulations, combining 4 values of M and β with at least 3 values of $\chi(p_c = 25)$ ($\in \{205.3, 107.5, 100.7\}\%$). Additional compressibility levels, $\chi(p_c = 25) \in \{127.1, 102.4\}\%$, are included for selected M and β combinations. In total, the study comprises 371 simulations.

Table 2. Flow and simulation properties of the numerical setup

Froude number	flow velocity	simulation duration	avalanche length
Fr	v_x	t_{max}	L
(-)	($\mathrm{m\,s^{-1}}$)	(s)	(m)
0.1	0.41	60 to 120	27.9 to 52.7
0.3	1.24	55 to 110	71.4 to 139.7
1	4.11	36.7	155.1
2	8.29	5 to 7.5	44.4 to 65.2
3	12.43	5 to 7.5	65.2 to 96.2
5	20.72	5 to 10	106.6 to 210.2
7	29.00	5 to 10	148.0 to 293.0

A sensitivity analysis with respect to grid resolution, slope angle, obstacle friction, and obstacle width is provided in the Supplementary Material S1. Results are robust with respect to grid resolution and slope angle. Obstacle friction has a measurable influence, with increasing friction leading to reduced run-up heights. The effect of obstacle width is discussed in Sect. 4.3. The Supplementary Material S2 contains simulation renderings showing characteristic flow morphology for every considered Fr and avalanche rheology.

2.3 Postprocessing

In the following, time-averaged values are denoted by an overline (e.g., $\bar{h}_\mathrm{r}$), peak values are denoted by a hat (e.g., $\hat{h}_\mathrm{r}$), and volume-averaged values by angle brackets (e.g., $\langle \sigma_{xx} \rangle$). We commonly normalize run-up and pressure height by the initial flow height H.

We determine run-up height h_r in each simulation frame as the maximum vertical position of the MPs within a centered $1.5\,\mathrm{m}$-wide strip upstream of the obstacle (cf. Fig. 2). Steady-state values are computed as the arithmetic mean over a time span, the temporal position of which is determined by a running deviation analysis. The time span is several seconds long and varies depending on the Froude number. Time history plots and the corresponding averaging time-spans are shown in Supplementary Material S3.

https://doi.org/10.5194/egusphere-2026-1181
Preprint. Discussion started: 7 April 2026

Impact pressure profiles are obtained by binning the MPs by their z-position at a resolution of $dx/2$ (cf. coordinate system in Fig. 2). For each bin, we compute the volume-average streamwise stress σ_{xx} within a domain directly upstream of the obstacle–avalanche interface. The domain extends from -0.5 to $2.5dx$ in the x-direction, from $\pm 0.75\,\mathrm{m}$ in the y-direction, and from 0 to $5H$ in the z-direction, resulting in 70 bins. The x-extent of $3dx$ was chosen to cover the compact support of the quadratic B-spline interpolation functions (cf. Appendix A2).

3 Dependence of run-up and impact pressure distribution on flow regime and material rheology

3.1 Run-Up height and its rheological contributors

Avalanche rheology controls run-up height differently depending on the flow regime. Fig. 3 (a) shows the time evolution of run-up height for a gravity-driven ($\mathrm{Fr} = 0.1$), a transitional ($\mathrm{Fr} = 1$), and an inertia-driven regime ($\mathrm{Fr} = 5$). The outermost curves form an envelope that captures the full variation due to these rheological differences. Within each regime, only the bulk rheological properties, internal friction, cohesion, and plastic compressibility vary. Since the material parameter ranges are identical across all cases (cf. Table 1), the spread of curves in each regime directly illustrates the effect of avalanche rheology on run-up height. Panel (b) in Fig. 3 is discussed at a later stage (Section 3.3). It presents a conceptually similar analysis to panel (a), but for a distinct quantity. We apply the same subfigure presentation in Fig. 3, Fig. 4, Fig. 7, and Fig. 10.

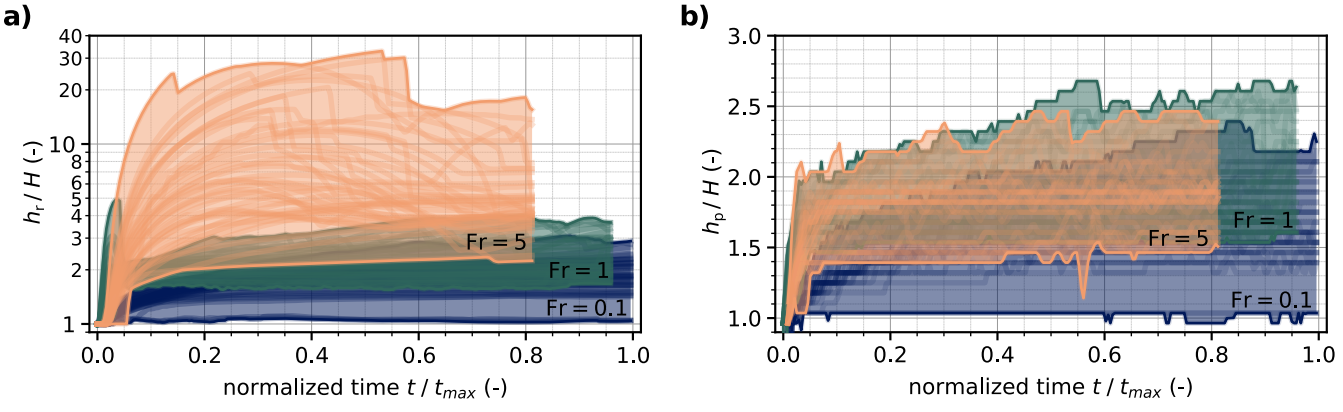

Figure 3. Envelopes of run-up height time histories (a) and pressure height (b) encompassing the whole range of varied material parameters (see Table 1) of a characteristic gravity-driven ($\mathrm{Fr} = 0.1$ in blue), a transitional ($\mathrm{Fr} = 1$ in green), and an inertia-driven regime ($\mathrm{Fr} = 5$ in orange). Curves for $\mathrm{Fr} = 1$ and $\mathrm{Fr} = 5$ are clipped for better visualization

Curves of the gravity-driven case ($\mathrm{Fr} = 0.1$) evolve smoothly toward a steady state, whereas curves of the transitional ($\mathrm{Fr} = 1$) and inertia-driven cases ($\mathrm{Fr} = 5$) exhibit initial peaks followed by the transition to steady conditions. These peaks originate from the rapid upward ejection of material at first contact with the obstacle. Because this idealized scenario assumes a uniformly deep flow with a vertical front, peak amplitudes may be sensitive to modeling simplifications; we therefore focus on steady-state

https://doi.org/10.5194/egusphere-2026-1181
Preprint. Discussion started: 7 April 2026

run-up heights, which are more robust. Ratios of peak to mean steady-state run-up heights for all simulated cases are documented in Supplementary Material S4.

In the steady-state, rheological variation has the strongest influence in the inertia-driven regime ($\mathrm{Fr} = 5$): the corresponding envelope spans run-up heights from about 2 to over 30 times the initial flow height (i.e., a factor of approximately 15). At lower Fr the spreads are considerably smaller: a factor of about 3 for the gravity-driven case ($\mathrm{Fr} = 0.1$) and a factor of 2.5 for the transitional case ($\mathrm{Fr} = 1$). This contrasts with impact pressure buildup, where inertial effects outweigh rheology-related contributions in inertia-driven flows (Kyburz et al., 2020; Kohler et al., 2025).

Analysis of the rheological-variation envelopes, however, does not isolate the contribution of individual rheological properties. In Figure 4 (a) we achieve this through a virtual rheological decomposition, progressively introducing friction, cohesion, and plastic compressibility starting from an inviscid, fluid-like baseline, presented as stacked $\bar{h}_\mathrm{r}(\mathrm{Fr})$ curves (similar to Kohler et al., 2025; Kyburz et al., 2020).

The inviscid, fluid-like curve closely follows the velocity head augmented by the flow height, confirming that formulations based on Bernoulli's principle offer a reasonable first-order description of run-up on narrow obstacles. Introducing granular rheology has a twofold effect on run-up height. At low Fr, friction and cohesion increase run-up through quasi-static pile-up, in which stronger internal resistance supports a higher material accumulation at the obstacle (cf. Gravish et al., 2010); at high Fr, friction and cohesion increase energy dissipation during the conversion from kinetic to potential energy, thereby reducing run-up height. Plastic compressibility has a minor influence compared to friction and cohesion. Decomposition plots for other rheological parameters, confirming the representativity of the selected ones, are provided in Supplementary Material S5.

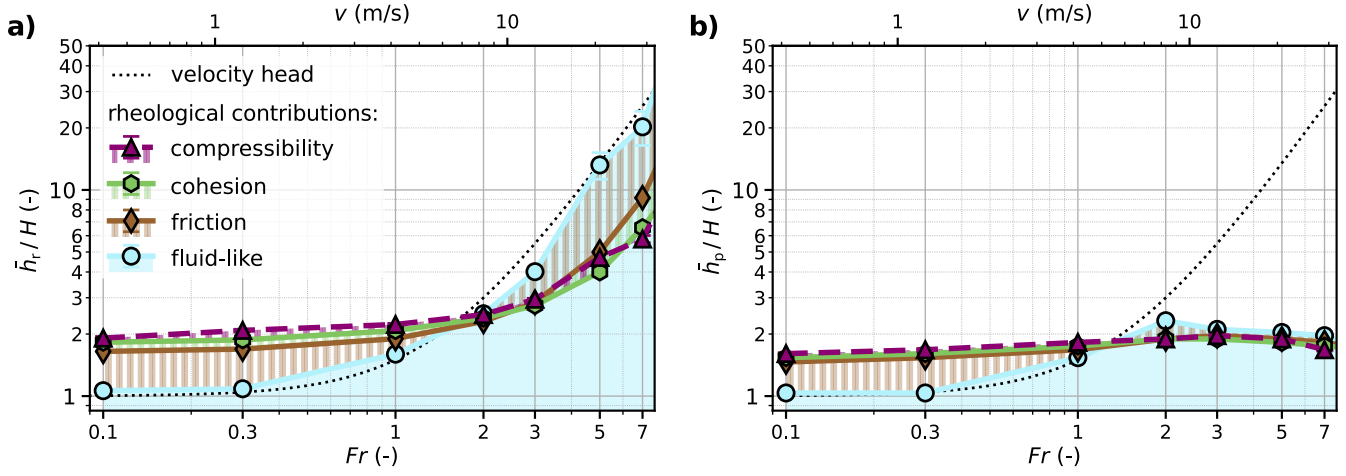

Figure 4. Run-up height (a) and pressure height (b) contributions from inviscid, fluid-like behavior, friction, cohesion, and plastic compressibility for $\mathrm{Fr} = 0.1$ to 7. Starting with the simulation of inviscid, fluid-like flows ($M = 0.0$, $\beta = 0.0$, $\chi(p_c = 25) = 100.7\%$), we progressively modify the corresponding material parameters to incorporate frictional, cohesive-frictional, and finally compressible cohesive-frictional behavior. The final material properties are $M = 0.8$, $\beta = 0.3$, $\chi(p_c = 25) = 107.5\%$. The velocity head (augmented by the addition of the flow height) is shown for reference

https://doi.org/10.5194/egusphere-2026-1181
Preprint. Discussion started: 7 April 2026

3.2 Impact pressure distribution and the concept of pressure height

185 In engineering practice, run-up height is commonly assumed to define the vertical extent of idealized impact pressure distributions on narrow obstacles. Our simulations show that this mixes up two distinct quantities. Figure 5 compares two exemplary time-averaged profiles of impact pressure for identical rheological properties but contrasting flow regimes: gravity-driven and inertia-driven.

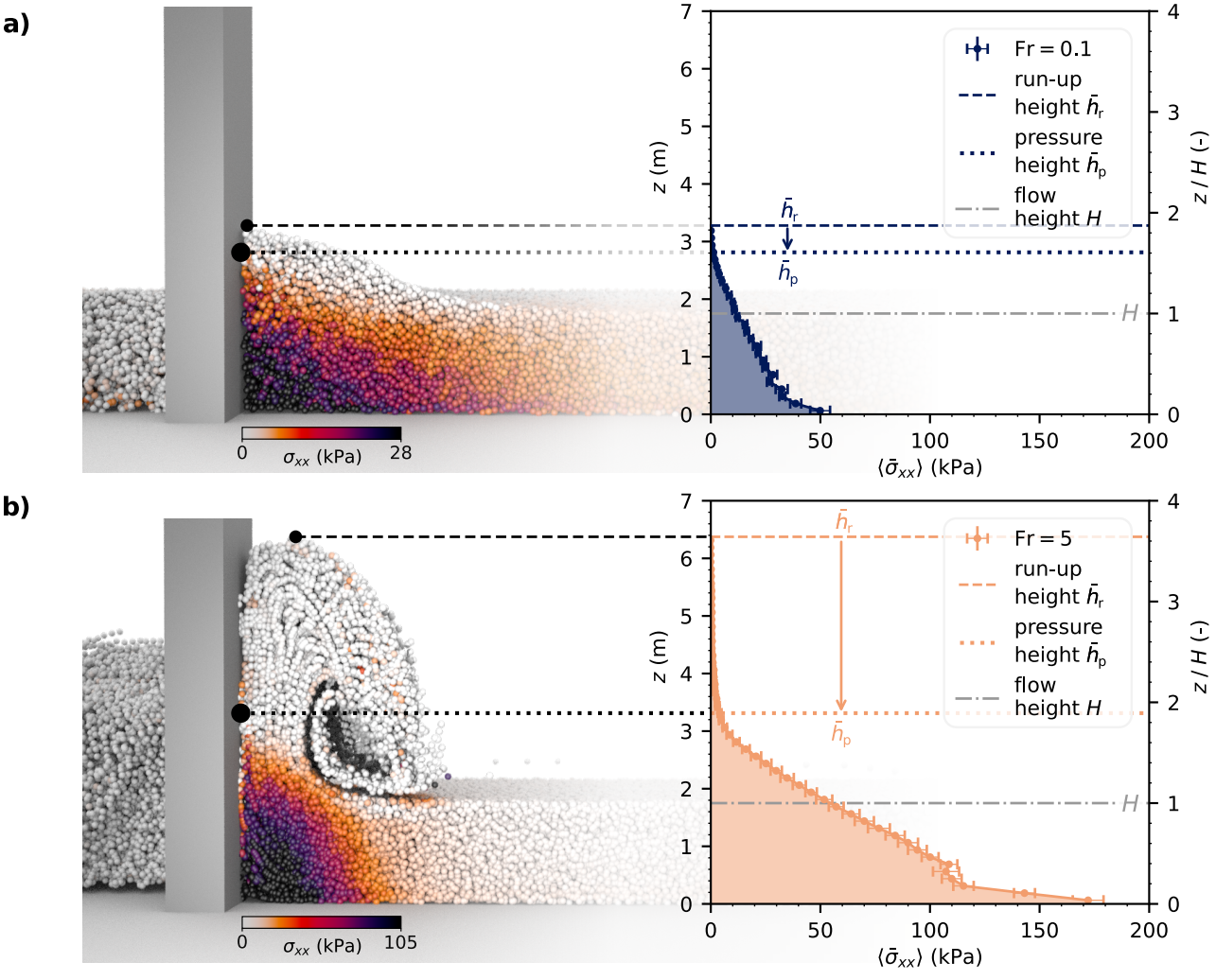

Figure 5. Longitudinal sections of two simulated avalanches (left) and the corresponding impact pressure profiles (right), highlighting the difference between run-up and pressure height. Material-Point colors indicate stream-wise stress σ_{xx}. Panel (a) shows a gravity-driven case ($\mathrm{Fr} = 0.1$), and panel (b) an inertia-driven case ($\mathrm{Fr} = 5$); both share identical avalanche rheology ($M = 0.8$, $\beta = 0.3$, $\chi(p_c = 25) = 107.5\%$).

https://doi.org/10.5194/egusphere-2026-1181
Preprint. Discussion started: 7 April 2026

In the gravity-driven case (Fig. 5 (a), $\mathrm{Fr} = 0.1$), significant pressure acts over a large fraction of the run-up height. In the inertia-driven case (Fig. 5 (b), $\mathrm{Fr} = 5$), the pressure distribution is confined to a much smaller height compared to the run-up height. To precisely quantify the vertical extent of significant impact pressure, we introduce the *pressure height* h_p. We define h_p as the height above the gliding surface ($z = 0$) at which the smoothed impact pressure profile $\sigma_{xx}(z)$ falls below 5% of the depth-averaged impact pressure within the flow height, $\langle \sigma_{xx} \rangle_H$. Profiles are smoothed using a second-order Savitzky–Golay filter with a 13-bin window (corresponding to a window height of $\approx 1.5\,\mathrm{m}$). Impact pressure profiles for other rheological parameters, confirming the representativity of the selected ones, are provided in Supplementary Material S6.

Figure 6 generalizes this finding across the full parameter space. At low Froude numbers, pressure height and run-up height remain of comparable magnitude. Above $\mathrm{Fr} \approx 2$, however, the two quantities diverge: while run-up continues to increase with Fr, pressure height saturates at approximately 1.5 to $2.5H$. This saturation is consistent with the laboratory observations of Hauksson et al. (2007) discussed in the introduction.

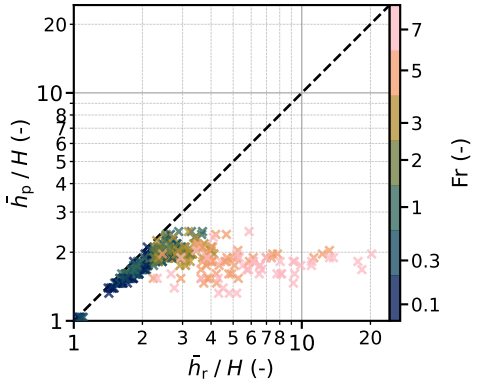

Figure 6. Pressure height over run-up height for the displayed Fr-range and the entire material parameter space constituted of M' and $\chi(p_c = 25)$

Another observation from Fig. 5 is that both flow regimes show increasing pressure toward the obstacle base. This is noteworthy in the inertia-driven case, where a uniform velocity profile would suggest an approximately uniform pressure distribution, given the proportionality between impact pressure and velocity in this regime (Kyburz et al., 2020). We attribute this to material deflection at a dead zone, creating a local pressure concentration that grows toward the base. This is consistent with flume experiments on inertia-driven flows reporting profiles of similar shape during the initial jet-formation stage of impact (Armanini et al., 2011).

3.3 Pressure height and its rheological contributors

In direct analogy to Sect. 3.1, we examine how flow regime and avalanche rheology control pressure height, first through pressure height time series, then through isolation of rheological contributions for mean steady-state values, and finally by identifying the governing mechanisms.

https://doi.org/10.5194/egusphere-2026-1181
Preprint. Discussion started: 7 April 2026

The pressure height time series in Fig. 3 (b) show that avalanche rheology has a more uniform influence on pressure height across all flow regimes than it does on run-up height. In steady state, the envelopes remain of similar magnitude across Froude numbers, merely showing a baseline shift from $\mathrm{Fr} = 0.1$ to the higher Froude numbers ($\mathrm{Fr} = 1$ and $\mathrm{Fr} = 5$). Unlike run-up, none of the curves exhibits pronounced transient peaks, regardless of flow regime or avalanche rheology (cf. Supplementary Material S4).

Applying the same virtual rheological decomposition as in Sect. 3.1 to obtain stacked $h_\mathrm{p}(\mathrm{Fr})$ curves, we find that up to $\mathrm{Fr} \approx 2$, pressure height behaves similarly to run-up height (cf. Fig. 4 (b)). The inviscid, fluid-like curve provides a baseline contribution, onto which frictional, cohesive, and plastic-compressibility effects add in a stacked manner. The influence of plastic compressibility is again minor compared to friction and cohesion. As for run-up height, we interpret this response as a quasi-static pile-up of material pushing against the obstacle. Beyond $\mathrm{Fr} \approx 2$, however, pressure height saturates with Fr, indicating a fundamental change in the governing mechanisms.

For the inviscid, fluid-like case, lateral fluxes, inherent to the three-dimensional nature of the present impact configuration, inhibit the formation of a persistent hydraulic jump, causing the pressure height to saturate. Under supercritical conditions, the incoming flow forms a vertical jet upon collision with the obstacle. For sufficiently wide obstacles, continued material accumulation ahead of the obstacle transforms the jet into a hydraulic jump (Armanini et al., 2011; Wu et al., 2023) that pushes statically against the obstacle, making pressure height equal to run-up height. For narrow obstacles, however, lateral fluxes inhibit this jump. The interaction remains deflection-driven, with particles deflected upward, losing streamwise velocity. Once that velocity approaches zero, momentum transfer to the obstacle diminishes while material continues to rise. Pressure height, therefore, saturates while run-up does not.

For granular rheologies, Fig. 4 (b) shows that pressure height becomes nearly independent of velocity, pointing to another mechanism. We attribute this to dead zone formation, a classical feature of granular impact that develops largely independently of flow velocity (Gray et al., 2003). At narrow, blunt obstacles, dead zones adopt wedge-shaped geometries (Tregaskis et al., 2022; Thibert et al., 2008), creating an internal interface between moving and static material where flow deflection occurs and impact pressures concentrate. The formation, shape, and persistence of the dead zone are controlled by granular rheology rather than velocity, which explains the observed velocity independence of pressure height. We further expect this mechanism to depend strongly on obstacle geometry, particularly the relative width w/H, as wider obstacles reduce lateral fluxes and sustain larger dead zones.

Together, these findings establish that dead zone formation and associated flow deflection govern pressure height on narrow obstacles, producing a behavior fundamentally different from run-up. Treating the two quantities as equivalent lacks physical justification, particularly in inertia-driven regimes.

4 Semi-empirical estimation of run-up and pressure height in avalanches

These physical distinctions motivate separate semi-empirical expressions for run-up and pressure height, each reflecting their respective governing mechanisms, while remaining in line with the spirit of the Swiss guidelines. Rather than reproducing the

https://doi.org/10.5194/egusphere-2026-1181
Preprint. Discussion started: 7 April 2026

full complexity of the three-dimensional simulations, the aim is to retain the dominant trends in a form suitable for engineering use.

The Swiss guidelines formulation for run-up height goes back to Salm et al. (1990), who formalized the velocity head from Bernoulli's principle Eq. (1) by introducing an empirical energy dissipation factor λ and a width-correction factor $f\left(\frac{w}{H}\right)$, yielding the expression

$$h_{\mathrm{r}} = \frac{h_v}{\lambda}\, f\left(\tfrac{w}{H}\right) = \frac{v^2}{2g\,\lambda}\, f\left(\tfrac{w}{H}\right). \tag{5}$$

λ depends on avalanche type, and $f\left(\frac{w}{H}\right)$ accounts for the obstacle width w relative to the incoming flow height H. The guidelines prescribe $\lambda = 1.5$ for dry, loose snow avalanches and $\lambda = 2$ to 3 for dense snow avalanches. The width-correction factor is given in tabular form and is well approximated by

$$f\left(\tfrac{w}{H}\right) = 1 - \exp\left(-1.14\,\frac{w}{H}\right). \tag{6}$$

We retain this structure but replace avalanche-type classifications with rheology-dependent parameters derived from our numerical results.

4.1 Semi-empirical modeling of run-up and pressure height

Both run-up and pressure height arise from the superposition of a gravity-driven pile-up and an inertia-driven contribution, motivating the additive decomposition

$$\bar{h}_i = \bar{h}_{i,\mathrm{gr}} + \bar{h}_{i,\mathrm{in}}, \tag{7}$$

where the index $i \in \{\,\mathrm{r},\mathrm{p}\,\}$ distinguishes between run-up (r) and pressure height (p). An additive decomposition of run-up height is also implicitly adopted in the Swiss guidelines, where the dynamic run-up height, obtained from Eq. (5), is measured relative to the avalanche surface and added to the flow height; this formulation, however, does not account for quasi-static pile-up.

We model the gravity-driven pile-up process identically for both quantities using the linear model

$$h_{i,\mathrm{gr}} = H(1+\zeta_i) \quad \text{with} \quad \zeta_i = k_i M'. \tag{8}$$

ζ_i is a magnification factor that quantifies the quasi-static pile-up process due to internal resistance. We model this effect solely through the effective internal friction M'; plastic compressibility is omitted for simplicity. The fitting parameter k_i controls the proportionality between M' and ζ_i for run-up and pressure height, respectively. For inviscid, fluid-like material behavior ($M' = 0$), Eq. (8) reduces to $h_{i,\mathrm{gr}} = H$ (i.e., $\zeta_i = 0$), consistent with experimental observations that subcritical water flows produce negligible run-up (Choi et al., 2015).

For the inertia-driven term, both run-up and pressure height follow the velocity head at low to moderate Fr. Run-up continues to scale with the velocity head at high Fr, whereas pressure height saturates beyond a characteristic Froude number (cf. Sect. 3.2). We capture this saturation by limiting the velocity head at a height threshold

$$h_{\mathrm{sat}} = \frac{\mathrm{Fr}_{\mathrm{sat}}^2\, H}{2}, \tag{9}$$

https://doi.org/10.5194/egusphere-2026-1181
Preprint. Discussion started: 7 April 2026

computed from the fitted Froude number at saturation $\mathrm{Fr}_{\mathrm{sat}}$. Here we use Eq. (1) and $\mathrm{Fr} = v/\sqrt{gH}$. The inertia-driven contributions are then written as

$$\bar{h}_{i,\mathrm{in}} = \begin{cases} \dfrac{h_v}{\lambda_i}, & \text{if} \quad i = \mathrm{r}, \\ \dfrac{\min(h_v, h_{\mathrm{sat}})}{\lambda_i}, & \text{if} \quad i = \mathrm{p}, \end{cases} \qquad \text{with} \quad \lambda_i = \exp(\kappa_i\, M'). \tag{10}$$

In direct analogy to Eq. (5), the factors λ_i represent energy dissipation factors. We model these factors as increasing exponentially with the effective internal friction M', with the rate controlled by parameter κ_i. The exponential form empirically matches the $h_i - M'$ trends presented in Appendix A3, and ensures $\lambda_i = 1$ for $M' = 0$, corresponding to the inviscid, fluid-like limit, while smoothly introducing friction-dependent dissipation for $M' > 0$. This replaces the avalanche-type classifications of Salm et al. (1990) with a continuous rheology-based parametrization.

Table 3. Regression coefficients for the run-up height and pressure height equation

(a) Run-up height equation

k_{r} (-)	κ_{r} (-)
0.95	1.57

RMSLE = 13.0 %

(b) Pressure height equation

k_{p} (-)	κ_{p} (-)	$\mathrm{Fr}_{\mathrm{sat}}$ (-)
0.53	1.31	1.54

NRMSE = 6.6 %

We determine the regression parameters using the `scipy.optimize.curve_fit` routine (Virtanen et al., 2020). The four-parameter dataset comprises the effective internal friction M', the plastic compressibility $\chi(p_c = 25)$, the flow velocity v, and the steady-state run-up $\bar{h}_{\mathrm{r}}$ or pressure height $\bar{h}_{\mathrm{p}}$, spanning the parameter ranges stated in Table 2 and Table 1, except for $\chi(p_c = 25) = 205.3\%$. The regression parameters and performance metrics are reported in Table 3. We assess the run-up model using the root mean square logarithmic error (RMSLE), given the quadratic velocity dependence of run-up height, and the pressure height model using the normalized root mean square error (NRMSE) (cf. Appendix A3.1). Figure 7 visualizes overall model performance. Both equations perform best for low to moderate plastic compressibilities. The run-up height equation shows slightly improved accuracy for intermediate effective internal friction ($M' \approx 0.4$ to 1.5); the accuracy of the pressure height equation shows no systematic dependence on M'. Across the full dataset, 92.9 % of simulated data points are predicted within $\pm 25\,\%$ by the run-up height equation; the pressure height equation captures $100\,\%$ of the data within the same tolerance band. These values are drawn from a more detailed evaluation of the model performance, included in Appendix A3.

The resulting $\lambda_i(M')$ and $\zeta_i(M')$ curves are shown in Fig. 8, with left ordinates giving the run-up height coefficients λ_{r} and ζ_{r} and right ordinates giving the pressure height coefficients λ_{p} and ζ_{p}.

https://doi.org/10.5194/egusphere-2026-1181
Preprint. Discussion started: 7 April 2026

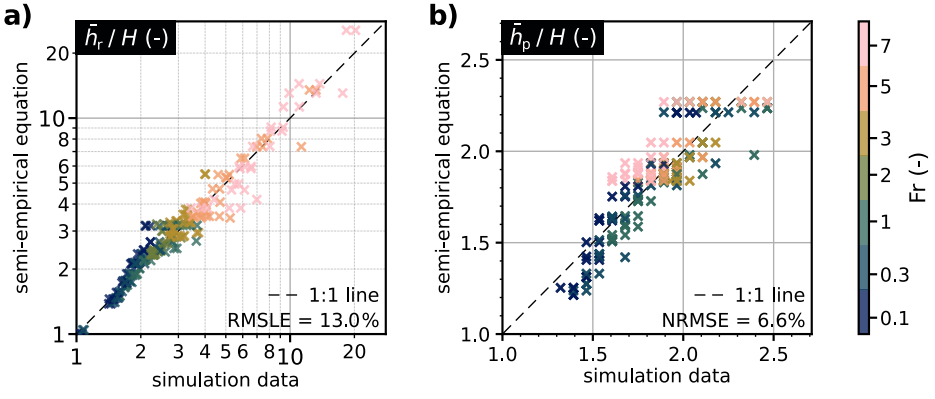

Figure 7. Semi-empirical equation for run-up height (a) and pressure height (b) vs. simulation results for the displayed Fr-range, spanning all simulated M' and $\chi(p_c = 25)$ values except $\chi(p_c = 25) = 205.3\%$

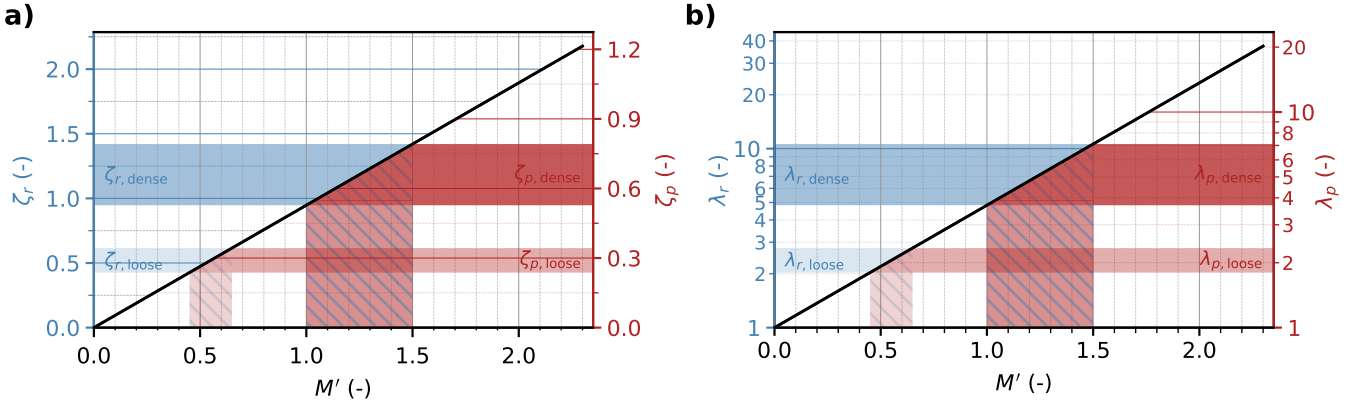

Figure 8. Quasi-static magnification factors ζ_r and ζ_p (a), and dissipation factors λ_r and λ_p (b) for run-up and pressure height, respectively, over the effective internal friction M'. The hatched areas mark the recommended value range for M' to match the run-up height of loose and dense snow avalanches from the Swiss guidelines (Margreth et al., 2015). Note the different ordinate scalings

https://doi.org/10.5194/egusphere-2026-1181
Preprint. Discussion started: 7 April 2026

4.2 Identification of rheological parameters

The dissipation factor λ in the Swiss guidelines was introduced as an empirical adjustment grounded in engineering judgment, not as a representation of a specific physical mechanism. Despite this empirical origin, the guidelines formulation provides a reasonable first-order description of run-up height for the prescribed λ values. We exploit this by identifying the values of M' for which our simulated run-up curves best match the guideline predictions, effectively translating λ into the physically meaningful parameter space of M'. This further allows established engineering knowledge for run-up estimation to be transferred to the pressure–height formulation proposed here.

To this end, we compare simulated $\bar{h}_r$–Fr curves for all considered avalanche rheologies against the guidelines recommendations, restricting the analysis to the inertia-driven regime ($3 \leq \mathrm{Fr} \leq 7$), since the guidelines equations lack a contribution from quasi-static pile-up. We quantify deviations between the simulated and guideline curves using the RMSLE as a function of M'.

The resulting RMSLE–M' curves are shown in Fig. 9 for both dry, loose snow avalanches and dense snow avalanches. In both cases, distinct minima indicate clear correspondences between the guideline dissipation factor λ and physically meaningful ranges of M' within our numerical framework. The correspondence is consistent for both nearly incompressible and moderately compressible configurations. For dry, loose snow avalanches ($\lambda = 1.5$), the best agreement occurs for $M' \approx 0.45$ to 0.65. Dense snow avalanches ($\lambda = 3$) correspond to higher friction levels, with $M' \approx 1.0$ to 1.5. These parameter ranges are marked in Fig. 8.

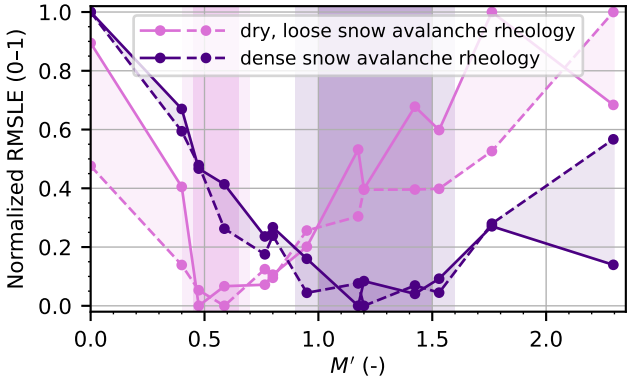

Figure 9. Deviation between simulated run-up height and the run-up height predicted by the Swiss guidelines for *dry, loose* and *dense* avalanche rheology (using $\lambda = 1.5$ and 3, respectively), plotted against the effective internal friction M'. The deviation is quantified using the RMSLE for each M', evaluated only for the inertia-driven regime ($3 \leq \mathrm{Fr} \leq 7$). The resulting RMSLE - M' curves are normalized to 0-1 to enable direct qualitative comparison. Continuous lines correspond to a nearly incompressible configuration ($\chi(p_c = 25) = 100.7\%$), whereas dashed lines represent a moderately compressible configuration ($\chi(p_c = 25) = 107.5\%$). Each avalanche rheology reveals a clear correspondence between the empirical dissipation factor λ used in the guidelines and a range of M' of the MPM model

https://doi.org/10.5194/egusphere-2026-1181
Preprint. Discussion started: 7 April 2026

4.3 Influence of relative obstacle width

The width-correction factor $f\left(\frac{w}{H}\right)$ reduces predicted run-up height for obstacles that are narrow relative to the flow height. We assess its validity within our numerical framework and test whether obstacle width affects run-up and pressure height similarly, using the rheological parameter ranges identified in Sect. 4.2 for dry, loose, and dense snow avalanche types.

For dry, loose snow avalanches, we use $M = 0.5$ and $\beta = 0.15$ (resulting in $M' = 0.59$) with $\chi(p_c = 25) = 107.5\,\%$, corresponding to moderate plastic compaction potential. For dense snow avalanches we use $M = 0.9$ and $\beta = 0.3$ (resulting in $M' = 1.32$) with $\chi(p_c = 25) = 102.4\,\%$, corresponding to small plastic compaction potential. In both cases, we vary the relative obstacle width over $w/H \in \{0.5, 1, 2, 3\}$. To sufficiently resolve narrow obstacles, we reduce the grid spacing to $dx = 0.125\,\mathrm{m}$. A sensitivity analysis confirms robustness with respect to grid resolution (cf. Supplementary Material S1).

Similar to the width-correction factor of the Swiss guidelines, we compute for each Fr

$$f_i\left(\tfrac{w}{H}\right) = \frac{\bar{h}_i\left(\tfrac{w}{H}\right)}{\bar{h}_i\left(\tfrac{w}{H} = 1\right)}, \tag{11}$$

which can be interpreted as a width-correction factor for run-up ($i = \mathrm{r}$) and pressure height ($i = \mathrm{p}$), relative to the reference case $w/H = 1$. Note that this definition differs slightly from the Swiss guideline, where the reference case corresponds to $w/H \geq 3$. We therefore rescale the guidelines function Eq. (6) such that it satisfies $f\left(\frac{w}{H}\right) = 1$ at $w/H = 1$.

Run-up height is only weakly sensitive to obstacle width across both avalanche types, with slightly more pronounced dependence for dense snow rheology (cf. Fig. 10, panels a.1 and a.2). Overall, the width correction of the Swiss guidelines marginally overestimates run-up height for $w/H > 1$ and marginally underestimates it for $w/H < 1$.

Pressure height is more sensitive to obstacle width, particularly in inertia-driven regimes ($\mathrm{Fr} = 3$ and $\mathrm{Fr} = 5$), where the numerical results closely follow the guidelines trend (cf. Fig. 10, panels b.1 and b.2). In gravity-driven ($\mathrm{Fr} = 0.1$) and transitional ($\mathrm{Fr} = 1$) regimes, the width dependence is substantially weaker. As for run-up height, the width correction of the Swiss guidelines marginally underestimates pressure height for $w/H < 1$.

For obstacles wider than the flow height ($w/H > 1$), the guidelines formulation is adequate: conservative for run-up height and accurate for pressure height. For narrower obstacles ($w/H < 1$), however, the simulations do not support the degree of reduction permitted by the guidelines. This is particularly relevant for slender structures such as cableway masts and transmission towers, where $w/H < 1$ is common.

5 Conclusions

This study examined the run-up and impact pressure distribution of snow avalanches impacting narrow obstacles, with two aims: clarifying the underlying physical mechanisms and improving how they are represented in engineering design practice. We addressed both through a comprehensive three-dimensional MPM parametric study, systematically varying flow regime and avalanche rheology.

Formulations based on the velocity head from Bernoulli's principle provide a reasonable first-order description of run-up height on narrow obstacles, provided that a rheology-dependent gravity-driven term is included and energy dissipation is quantified

https://doi.org/10.5194/egusphere-2026-1181
Preprint. Discussion started: 7 April 2026

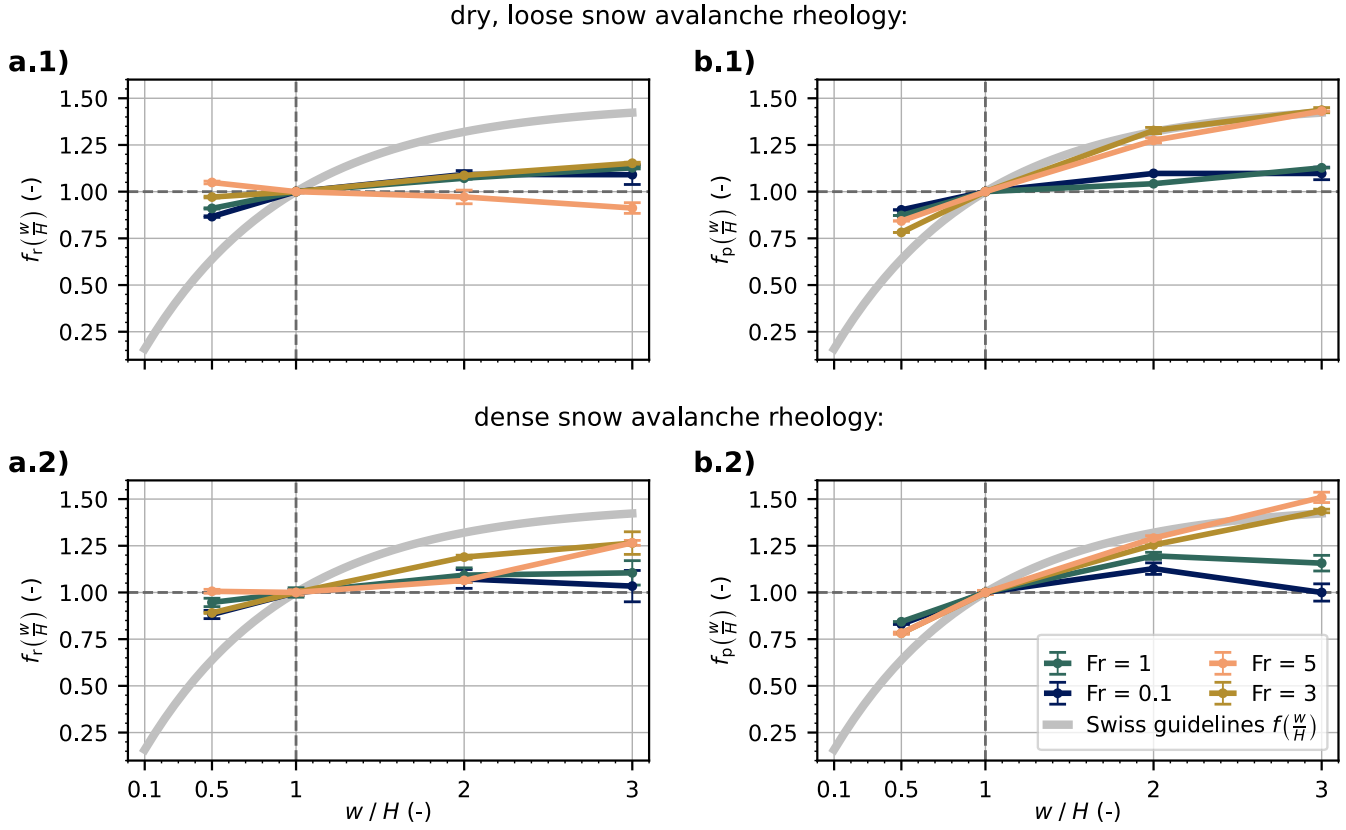

Figure 10. Width-correction factors $f_i\left(\frac{w}{H}\right)$ for run-up height ($i = \mathrm{r}$, left column) and for pressure height ($i = \mathrm{p}$, right column) plotted over the normalized obstacle width w/H. The upper row (panels a.1 and b.1) corresponds to dry, loose snow avalanche rheology ($\chi(p_c = 25) = 107.5\,\%$, $M = 0.5$, $\beta = 0.15$; $M' = 0.59$), and the lower row (panels a.2 and b.2) corresponds to dense snow avalanche rheology ($\chi(p_c = 25) = 102.4\,\%$, $M = 0.9$, $\beta = 0.3$; $M' = 1.32$), following Sect. 4.2.

through rheological properties. Friction and cohesion increase quasi-static pile-up in gravity-driven regimes but act dissipatively at higher Froude numbers, reducing inertia-driven run-up. Building on these trends, we proposed semi-empirical extensions of the Swiss guidelines velocity-head formulation, continuously parameterized through the effective internal friction. Within this framework, the empirical avalanche-type dependent dissipation factors prescribed in the guidelines map systematically to distinct ranges of effective internal friction in our constitutive model. These are $M' \approx 0.45$ to 0.65 for dry, loose snow avalanches and $M' \approx 1.0$ to 1.5 for dense snow avalanches.

A central finding is that run-up height is not a reliable indicator of the vertical extent of significant impact pressure, particularly in inertia-driven regimes. While run-up may reach several flow heights, significant impact pressure remains confined to a much smaller extent, typically a few flow heights. We introduced pressure height as a distinct measure of this effective load height. Unlike run-up, pressure height is governed primarily by flow deflection at a dead zone near the obstacle base. These processes

https://doi.org/10.5194/egusphere-2026-1181
Preprint. Discussion started: 7 April 2026

are primarily controlled by avalanche rheology rather than flow velocity. Even for inviscid, fluid-like rheology, pressure height saturates at a characteristic Froude number, marking the onset of supercritical conditions. For practical application of these findings, assuming a maximum pressure height of approximately three flow heights provides a conservative approximation, consistent with the experimental observations of Hauksson et al. (2007).

Width effects are most pronounced for pressure height in inertia-driven regimes and negligible in gravity-driven regimes. The Swiss guidelines width-correction factor is adequate for obstacles wider than the flow height. For narrower obstacles, the configuration typical of cableway masts and transmission towers, our results do not support the magnitude of reduction prescribed by the guidelines for either run-up or pressure height, and we recommend limiting $f\left(\frac{w}{H}\right)$ to a minimum of 0.7 for $w/H < 1$.

This study builds on several simplifying assumptions that limit its scope. The analysis is restricted to plug flow velocity profiles, whereas many avalanche flow regimes exhibit pronounced shear (Köhler et al., 2018). Only dense, granular snow avalanches are considered; effects related to powder snow avalanches are beyond the scope of this work. The study is further confined to stationary conditions, yet temporal variability in flow height, velocity, or density are principal sources of uncertainty in avalanche impact (Jóhannesson et al., 2009). The proposed formulations, despite being grounded in systematic rheological analysis, remain semi-empirical; a closed analytical treatment appears difficult to achieve for three-dimensional impact problems. Semi-empirical approaches supplemented by three-dimensional simulations, however, offer a pragmatic path toward more general methods.

These limitations point directly to the most pressing directions for future work. Extending the framework to sheared or unsteady inflow conditions would remove the two most restrictive assumptions. A dedicated geometrical parametric study, varying obstacle width, flow height, and cross-sectional shape independently, could clarify the role of flow height and test the universality of Froude number scaling. Such a study would also provide the empirical basis needed to derive shape-dependent correction factors for run-up, analogous to the geometric drag coefficients established for impact pressure (Kyburz et al., 2022). Transient peak run-up and the vertical loading on protruding structural elements also offer promising ground for numerical and experimental investigation.

Code and data availability. The main raw time-series data, a post-processing script reproducing the key figures, and the regression of the equations will be made publicly available in a dedicated repository on Zenodo under the Avalanche Dynamics community: https://zenodo.org/communities/avalanche-dynamics/records

Author contributions. Michael J. Kohler: Writing – original draft, Visualization, Validation, Methodology, Investigation, Formal analysis, Data curation, Conceptualization. Johan Gaume: Writing – review & editing, Validation, Supervision, Software, Methodology, Investigation, Conceptualization. Christophe Ancey: Writing – review & editing, Supervision. Betty Sovilla: Writing – review & editing, Supervision, Resources, Project administration, Methodology, Investigation, Funding acquisition, Conceptualization.

https://doi.org/10.5194/egusphere-2026-1181
Preprint. Discussion started: 7 April 2026

Competing interests. The authors declare that they have no conflict of interest.

Acknowledgements. During the preparation of this manuscript, the authors used Large Language Models (ChatGPT and Claude) and DeepL to assist with improving language and readability. All content generated or modified using these tools was carefully reviewed and edited by the authors, who take full responsibility for the final manuscript. No AI tools were used for the interpretation of the results or for drawing scientific conclusions.

Appendix A

A1 Derivation of the plastic compressibility parameter

The plastic compressibility parameter $\chi(p_c = 25)$ serves as a density-increase factor (in %) that quantifies how much the material densifies under compression at a reference pre-consolidation pressure of $25\,\mathrm{kPa}$. We derive it by rearranging Eq. (4):

$$J_P(p_c) = \exp\left(-\sinh^{-1}(p_c/K)/\xi\right), \tag{A1}$$

where $J_P = \exp \varepsilon_V^P$. Using $\chi = 1/J_P = \rho/\rho_0$ and evaluating at $p_c = 25\,\mathrm{kPa}$ yields

$$\chi(p_c = 25) = J_P(p_{c,0}) \,/\, J_P(25\,\mathrm{kPa}), \tag{A2}$$

where the numerator corresponds to the initial kinematic configuration under the initial pre-consolidation pressure $p_{c,0}$.

A2 Volume-Averaging Procedure

A MP property x is volume-averaged within a domain D by weighting the individual property of each MP i with its Jacobian J_i through

$$\langle x \rangle_D = \frac{\sum_{i=1}^{n} x_i J_i}{\sum_{i=1}^{n} J_i}, \tag{A3}$$

where n is the number of MPs in the averaging domain. Here we use the angle brackets to denote volume-averaged quantities. For impact pressure, which we define as the flow-wise component σ_{xx} of the Cauchy stress tensor, this relation simplifies to

$$\langle \sigma_{xx} \rangle_D = \frac{\sum_{i=1}^{n} \tau_{xx,i}}{\sum_{i=1}^{n} J_i}, \tag{A4}$$

where we utilized the identity $\boldsymbol{\sigma} = \boldsymbol{\tau}/J$.

To calculate a depth-averaged impact pressure we perform this procedure in the *impact domain*. This fixed volume extends almost over the entire width of the obstacle ($1.5\,\mathrm{m}$) and its height matches the initial flow height of $1.75\,\mathrm{m}$. The upstream extent reaches from $x = -0.5dx$ to $x = 2.5dx$ and was selected to (i) cover the one-sided range of the cubic B-spline interpolation functions amounting $2dx$ a visualized in Figure A1 and (ii) capture the particles which slightly penetrate the obstacle, which is commonly observed in MPM.

https://doi.org/10.5194/egusphere-2026-1181
Preprint. Discussion started: 7 April 2026

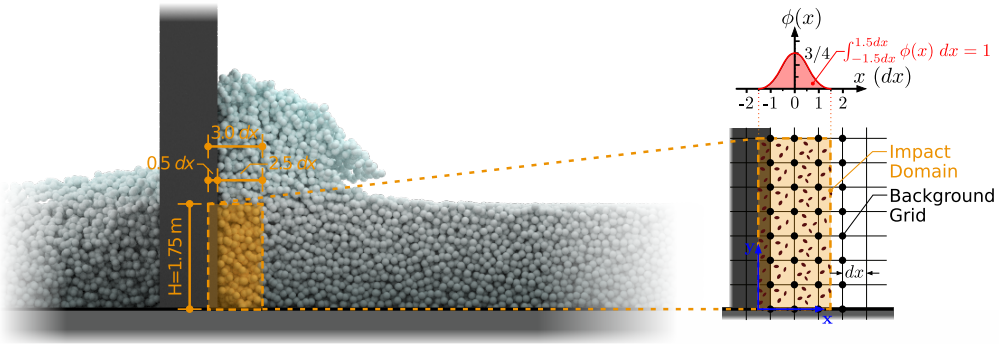

Figure A1. Illustration of the impact domain, showing the cubic B-spline interpolation functions and their extend at an exemplary MP in the x-direction (taken from Kohler et al. (2025))

For a volume-averaged compaction measure, it proved more robust to track the total mass of all particles within the impact region, excluding the portion that extends into the obstacle. We then divide this mass by the volume of the region and compare it to the original (reference) density.

A3 Semi-Empirical Modeling

A3.1 Performance Metrics

Let $\{y_i\}_{i=1}^n$ denote the simulated values and $\{f_i\}_{i=1}^n$ the corresponding predictions from the semi-empirical equations, with $\bar{y} = \frac{1}{n}\sum_{i=1}^n y_i$ and $\overline{\log y} = \frac{1}{n}\sum_{i=1}^n \log y_i$. All logarithms are natural. We assume $y_i, f_i > 0$ throughout.

The following metrics assess goodness of fit in both linear and logarithmic space, capturing overall accuracy, systematic bias, and the fraction of predictions falling within specified relative tolerances. The run-up height equation is fitted and evaluated in log-space; the pressure height equation in linear space.

- Coefficient of Determination in linear space (R^2):

$$R^2 = 1 - \frac{\sum_{i=1}^n (y_i - f_i)^2}{\sum_{i=1}^n (y_i - \bar{y})^2}.$$

  Fraction of variance in the simulated values explained by the predictions. Used to evaluate the pressure height equation.

- Coefficient of Determination in log–log space ($R^2_{\log}$):

$$R^2_{\log} = 1 - \frac{\sum_{i=1}^n (\log y_i - \log f_i)^2}{\sum_{i=1}^n (\log y_i - \overline{\log y})^2}.$$

  Analogous to R^2, applied to log-transformed values. Used to evaluate the run-up height equation.

https://doi.org/10.5194/egusphere-2026-1181
Preprint. Discussion started: 7 April 2026

- Mean Normalized Root Mean Square Error (NRMSE):

$$\mathrm{NRMSE}_{\mathrm{mean}} = \frac{1}{\bar{y}}\sqrt{\frac{1}{n}\sum_{i=1}^{n}(y_i - f_i)^2}.$$

RMSE expressed as a fraction of the sample mean, giving a scale-independent measure of linear-space error. Used to evaluate the pressure height equation.

- Root Mean Square Logarithmic Error (RMSLE):

$$\mathrm{RMSLE} = \sqrt{\frac{1}{n}\sum_{i=1}^{n}(\log y_i - \log f_i)^2}.$$

RMS error in log-space, equivalent to the RMS of the log-ratios $\log(y_i/f_i)$. Approximates a typical relative error when errors are small. Used to evaluate the run-up height equation.

- Multiplicative Bias Factor:

$$\mathrm{Bias}_{\times} = \exp\left(\frac{1}{n}\sum_{i=1}^{n}\log\frac{y_i}{f_i}\right).$$

Geometric mean of the ratio y_i/f_i. Values above unity indicate systematic under-prediction; values below unity indicate over-prediction.

- Agreement Fractions:

$$\mathrm{Frac}_p = \frac{1}{n}\sum_{i=1}^{n}\mathbf{1}\left(\frac{|y_i - f_i|}{y_i} \le p\right), \quad p \in \{0.10, 0.25\}.$$

Proportion of predictions within a relative tolerance p of the simulated value.

A3.2 Run-Up Height

Figure A3 shows how prediction accuracy varies with Fr, M', and $\chi(p_c = 25)$. The equation performs best for low to moderate plastic compressibility. For $\chi(p_c = 25) = 100.7\%$, RMSLE remains mostly below $10\,\%$ for $\mathrm{Fr} < 3$, rising to $10\,\%$ to $15\,\%$ for $3 \le \mathrm{Fr} \le 7$. For $\chi(p_c = 25) = 107.5\%$, errors are slightly larger: $7\,\%$ to $15\,\%$ for $\mathrm{Fr} < 3$ and $14\,\%$ to $23\,\%$ for $3 \le \mathrm{Fr} \le 7$. For the highly compressible case ($\chi(p_c = 25) = 205.3\%$), which lies outside the fitting range, the equation is only reliable for $\mathrm{Fr} < 3$, where RMSLE stays below $20\,\%$. Across all compressibilities, accuracy is best for intermediate effective internal friction, $M' = 0.4$ to 1.5, where RMSLE remains at or below $10\,\%$.

A3.3 Pressure Height

Figure A5 shows how prediction accuracy varies with Fr, M', and $\chi(p_c = 25)$. As for the run-up equation, accuracy is best for low to moderate plastic compressibility. For $\chi(p_c = 25) = 100.7\%$, NRMSE remains between $4\,\%$ to $8\,\%$ across the full Fr

https://doi.org/10.5194/egusphere-2026-1181
Preprint. Discussion started: 7 April 2026

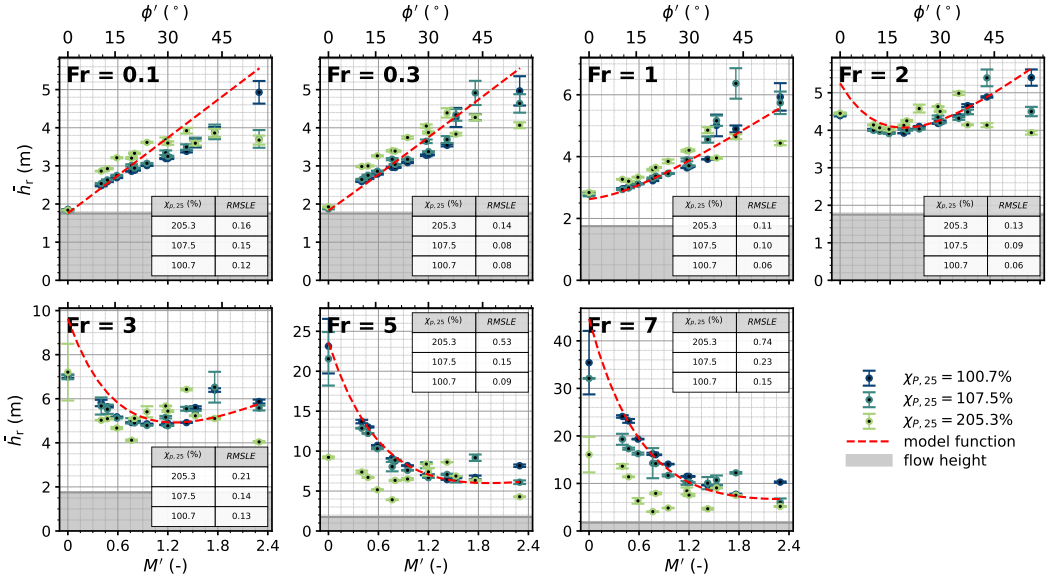

Figure A2. Run-up height over effective internal friction for three different compressibilities

Table A1. Regression coefficients and associated statistics of the run-up height equation. A Bias of 0.981, translates to an over-prediction of ≈1.9%

Parameter	Value	Rel. Std. Error	t-Statistic	p-Value
k_r (-)	0.9468	0.0457	21.888	0.0
κ_r (-)	1.5745	0.0188	53.300	0.0

Global metrics	
$R^2_{\log}$	0.939
RMSLE	0.130
$\text{Bias}_\times$	0.981
Frac_{10}	66.3%
Frac_{25}	92.9%

range. For $\chi(p_c = 25) = 107.5\%$, errors are slightly larger, reaching up to $14\,\%$ at high Fr. For the highly compressible case ($\chi(p_c = 25) = 205.3\%$), NRMSE exceeds $20\,\%$ for $\text{Fr} > 3$ and $M' < 0.4$. Across all compressibilities, the equation performs well for $M' \geq 0.4$, where NRMSE remains below $10\,\%$.

https://doi.org/10.5194/egusphere-2026-1181
Preprint. Discussion started: 7 April 2026

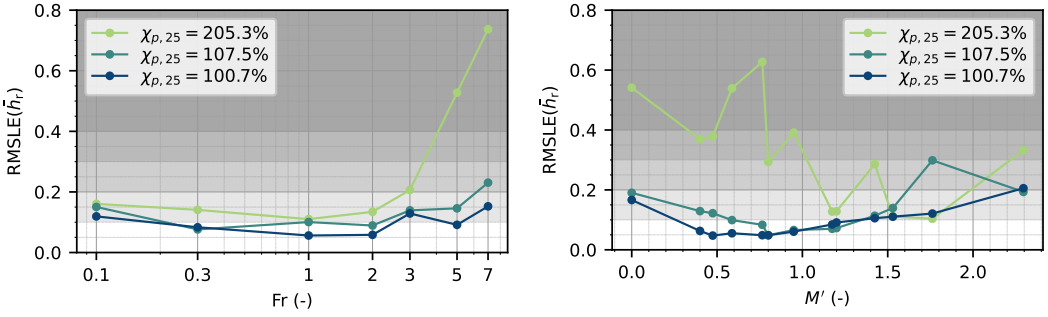

Figure A3. Left panel: RMSLE over the M' range, plotted over Fr. Right panel: RMSLE over the Fr range, plotted over M'

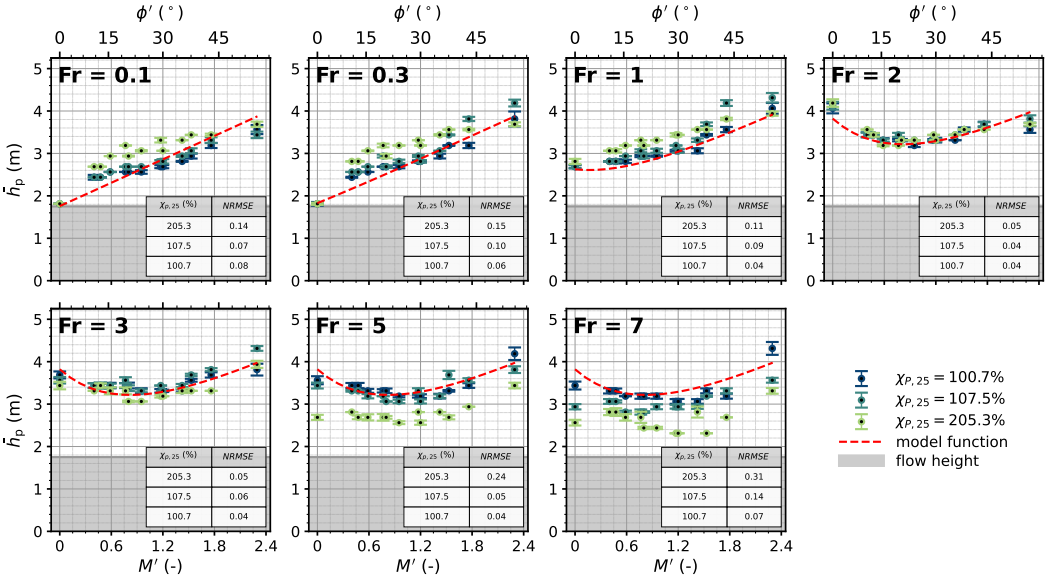

Figure A4. Pressure height over effective internal friction for three different compressibilities

Table A2. Regression coefficients and associated statistics of the pressure height equation. A Bias of 1.011, translates to an under-prediction of ≈1.1%

Parameter	Value	Rel. Std. Error	t-Statistic	p-Value
$\boldsymbol{k_p}$ (-)	0.5277	0.0186	53.893	0.0
$\mathbf{Fr_{sat}}$ (-)	1.5380	0.0370	27.052	0.0
$\boldsymbol{\kappa_p}$ (-)	1.3072	0.0924	10.819	0.0

Global metrics	
R^2	0.752
$\mathrm{NRMSE_{mean}}$	0.066
$\mathrm{Bias_{\times}}$	1.011
$\mathrm{Frac_{10}}$	85.2%
$\mathrm{Frac_{25}}$	100.0%

https://doi.org/10.5194/egusphere-2026-1181
Preprint. Discussion started: 7 April 2026

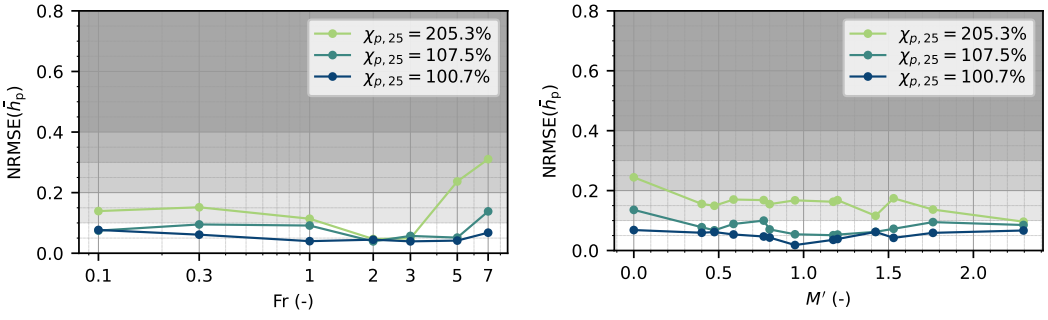

Figure A5. Left panel: NRMSE over the M' range, plotted over Fr. Right panel: NRMSE over the Fr range, plotted over M'

https://doi.org/10.5194/egusphere-2026-1181
Preprint. Discussion started: 7 April 2026

References

Armanini, A., Larcher, M., and Odorizzi, M.: Dynamic Impact of a Debris Flow Front against a Vertical Wall, Italian journal of engineering geology and environment, pp. 1041–1049, https://doi.org/10.4408/IJEGE.2011-03.B-113, 2011.

Bartelt, P., Caviezel, A., Degonda, S., and Buser, O.: Avalanche Impact Pressures on Structures with Upstream Pile-Up/Accumulation Zones of Compacted Snow, Natural Hazards and Earth System Sciences Discussions, pp. 1–16, https://doi.org/10.5194/nhess-2018-154, 2018.

Blatny, L., Löwe, H., Wang, S., and Gaume, J.: Computational Micromechanics of Porous Brittle Solids, Computers and Geotechnics, 140, 104 284, https://doi.org/10.1016/j.compgeo.2021.104284, 2021.

Choi, C. E., Au-Yeung, S. C. H., Ng, C. W. W., and Song, D.: Flume Investigation of Landslide Granular Debris and Water Runup Mechanisms, Géotechnique Letters, 5, 28–32, https://doi.org/10.1680/geolett.14.00080, 2015.

Eidevåg, T., Thomson, E. S., Kallin, D., Casselgren, J., and Rasmuson, A.: Angle of Repose of Snow: An Experimental Study on Cohesive Properties, Cold Regions Science and Technology, 194, 103 470, https://doi.org/10.1016/j.coldregions.2021.103470, 2022.

Faug, T.: Macroscopic Force Experienced by Extended Objects in Granular Flows over a Very Broad Froude-number Range, The European Physical Journal E, 38, 34, https://doi.org/10.1140/epje/i2015-15034-3, 2015.

Faug, T.: Impact Force of Granular Flows on Walls Normal to the Bottom: Slow versus Fast Impact Dynamics, Canadian Geotechnical Journal, 58, 114–124, https://doi.org/10.1139/cgj-2019-0399, 2021.

Faug, T., Chanut, B., Beguin, R., Naaim, M., Thibert, E., and Baroudi, D.: A Simple Analytical Model for Pressure on Obstacles Induced by Snow Avalanches, Annals of Glaciology, 51, 1–8, https://doi.org/10.3189/172756410791386481, 2010.

Gaume, J., Gast, T., Teran, J., van Herwijnen, A., and Jiang, C.: Dynamic Anticrack Propagation in Snow, Nature Communications, 9, 3047, https://doi.org/10.1038/s41467-018-05181-w, 2018.

Gravish, N., Umbanhowar, P. B., and Goldman, D. I.: Force and Flow Transition in Plowed Granular Media, Physical Review Letters, 105, 128 301, https://doi.org/10.1103/PhysRevLett.105.128301, 2010.

Gray, J. M. N. T., Tai, Y.-C., and Noelle, S.: Shock Waves, Dead Zones and Particle-Free Regions in Rapid Granular Free-Surface Flows, Journal of Fluid Mechanics, 491, 161–181, https://doi.org/10.1017/S0022112003005317, 2003.

Hákonardóttir, K. M.: A Laboratory Study of the Interaction between Supercritical, Shallow Flows and Dams, no. 03038 in Greinargerð / Veðurstofa Íslands, Veðurstofa Íslands, Reykjavík, 2003.

Hauksson, S., Pagliardi, M., Barbolini, M., and Jóhannesson, T.: Laboratory Measurements of Impact Forces of Supercritical Granular Flow against Mast-like Obstacles, Cold Regions Science and Technology, 49, 54–63, https://doi.org/10.1016/j.coldregions.2007.01.007, 2007.

Iverson, R. M., George, D. L., and Logan, M.: Debris Flow Runup on Vertical Barriers and Adverse Slopes, Journal of Geophysical Research: Earth Surface, 121, 2333–2357, https://doi.org/10.1002/2016JF003933, 2016.

Jóhannesson, T., Gauer, P., Issler, D., and Lied, K., eds.: The Design of Avalanche Protection Dams - Recent Practical and Theoretical Developments, Publications Office of the European Union, Brussels, https://doi.org/doi/10.2777/12871, 2009.

Köhler, A., McElwaine, J. N., and Sovilla, B.: GEODAR Data and the Flow Regimes of Snow Avalanches, Journal of Geophysical Research: Earth Surface, 123, 1272–1294, https://doi.org/10.1002/2017JF004375, 2018.

Kohler, M. J., Gaume, J., Ancey, C., and Sovilla, B.: 3D Numerical Modeling of Compressible and Cohesive Granular Flow Impact on Narrow Obstacles, 2025.

https://doi.org/10.5194/egusphere-2026-1181
Preprint. Discussion started: 7 April 2026

Kyburz, M. L., Sovilla, B., Gaume, J., and Ancey, C.: Decoupling the Role of Inertia, Friction, and Cohesion in Dense Granular Avalanche Pressure Build-up on Obstacles, Journal of Geophysical Research: Earth Surface, 125, e2019JF005 192, https://doi.org/10.1029/2019JF005192, 2020.

Kyburz, M. L., Sovilla, B., Gaume, J., and Ancey, C.: Physics-Based Estimates of Drag Coefficients for the Impact Pressure Calculation of Dense Snow Avalanches, Engineering Structures, 254, 113 478, https://doi.org/10.1016/j.engstruct.2021.113478, 2022.

Kyburz, M. L., Sovilla, B., Bühler, Y., and Gaume, J.: Potential and Challenges of Depth-Resolved Three-Dimensional MPM Simulations: A Case Study of the 2019 'Salezer' Snow Avalanche in Davos, Annals of Glaciology, pp. 1–14, https://doi.org/10.1017/aog.2024.14, 2024.

Li, X., Sovilla, B., Jiang, C., and Gaume, J.: The Mechanical Origin of Snow Avalanche Dynamics and Flow Regime Transitions, The Cryosphere, 14, 3381–3398, https://doi.org/10.5194/tc-14-3381-2020, 2020.

Li, X., Sovilla, B., Jiang, C., and Gaume, J.: Three-Dimensional and Real-Scale Modeling of Flow Regimes in Dense Snow Avalanches, Landslides, 18, https://doi.org/10.1007/s10346-021-01692-8, 2021.

Li, X., Sovilla, B., Gray, J. M. N. T., and Gaume, J.: Transient Wave Activity in Snow Avalanches Is Controlled by Entrainment and Topography, Communications Earth & Environment, 5, 1–11, https://doi.org/10.1038/s43247-023-01157-x, 2024.

Lin, B., Wu, Y., Niu, Z., and Wang, D.: Flow Jump Regimes of Inclined Granular Flow Interacting with Downstream Wall-like Obstacle, Powder Technology, 465, 121 342, https://doi.org/10.1016/j.powtec.2025.121342, 2025.

Margreth, S., Stoffel, L., and Schaer, M.: Berücksichtigung der Lawinen- und Schneedruckgefährdung bei Seilbahnen. Ein Leitfaden für die Praxis, WSL Berichte, 2015.

Mcclung, D. M. and Mears, A. I.: Dry-Flowing Avalanche Run-up and Run-Out, Journal of Glaciology, 41, 359–372, https://doi.org/10.3189/S0022143000016233, 1995.

Mejean, S., Faug, T., and Einav, I.: A General Relation for Standing Normal Jumps in Both Hydraulic and Dry Granular Flows, Journal of Fluid Mechanics, 816, 331–351, https://doi.org/10.1017/jfm.2017.82, 2017.

Ortiz, M. and Pandolfi, A.: A Variational Cam-clay Theory of Plasticity, Computer Methods in Applied Mechanics and Engineering, 193, 2645–2666, https://doi.org/10.1016/j.cma.2003.08.008, 2004.

Ortner, G., Bründl, M., Kropf, C. M., Röösli, T., Bühler, Y., and Bresch, D. N.: Large-Scale Risk Assessment on Snow Avalanche Hazard in Alpine Regions, Natural Hazards and Earth System Sciences, 23, 2089–2110, https://doi.org/10.5194/nhess-23-2089-2023, 2023.

Ritter, J., Löwe, H., and Gaume, J.: Microstructural Controls of Anticrack Nucleation in Highly Porous Brittle Solids, Scientific Reports, 10, 12 383, https://doi.org/10.1038/s41598-020-67926-2, 2020.

Roscoe, K. H. and Burland, J. B.: On the Generalised Stress-Strain Behaviour of 'Wet' Clay, Engineering Plasticity, pp. 535–609, 1968.

Rudolf-Miklau, F., Sauermoser, S., and Mears, A. I., eds.: The Technical Avalanche Protection Handbook, Wiley, 1 edn., https://doi.org/10.1002/9783433603840, 2014.

Salm, B., Burkard, A., and Gubler, H. U.: Berechnung von Fliesslawinen. Eine Anleitung fuer Praktiker mit Beispielen, Tech. Rep. 47, Eidgenössisches Institut für Schnee- und Lawinenforschung, Weissfluhjoch/Davos, 1990.

Simo, J. C. and Meschke, G.: A New Class of Algorithms for Classical Plasticity Extended to Finite Strains. Application to Geomaterials, Computational Mechanics, 11, 253–278, https://doi.org/10.1007/BF00371865, 1993.

Sovilla, B., Schaer, M., Kern, M., and Bartelt, P.: Impact Pressures and Flow Regimes in Dense Snow Avalanches Observed at the Vallée de La Sionne Test Site, Journal of Geophysical Research: Earth Surface, 113, https://doi.org/10.1029/2006JF000688, 2008a.

Sovilla, B., Schaer, M., and Rammer, L.: Measurements and Analysis of Full-Scale Avalanche Impact Pressure at the Vallée de La Sionne Test Site, Cold Regions Science and Technology, 51, 122–137, https://doi.org/10.1016/j.coldregions.2007.05.006, 2008b.

https://doi.org/10.5194/egusphere-2026-1181
Preprint. Discussion started: 7 April 2026

Stomakhin, A., Schroeder, C., Chai, L., Teran, J., and Selle, A.: A Material Point Method for Snow Simulation, ACM Transactions on Graphics, 32, 102:1–102:10, https://doi.org/10.1145/2461912.2461948, 2013.

Sulsky, D., Chen, Z., and Schreyer, H. L.: A Particle Method for History-Dependent Materials, Computer Methods in Applied Mechanics and Engineering, 118, 179–196, https://doi.org/10.1016/0045-7825(94)90112-0, 1994.

Techel, F., Jarry, F., Kronthaler, G., Mitterer, S., Nairz, P., Pavšek, M., Valt, M., and Darms, G.: Avalanche Fatalities in the European Alps: Long-Term Trends and Statistics, Geographica Helvetica, 71, 147–159, https://doi.org/10.5194/gh-71-147-2016, 2016.

Thibert, E., Baroudi, D., Limam, A., and Berthet-Rambaud, P.: Avalanche Impact Pressure on an Instrumented Structure, Cold Regions Science and Technology, 54, 206–215, https://doi.org/10.1016/j.coldregions.2008.01.005, 2008.

Tregaskis, C., Johnson, C. G., Cui, X., and Gray, J. M. N. T.: Subcritical and Supercritical Granular Flow around an Obstacle on a Rough Inclined Plane, Journal of Fluid Mechanics, 933, A25, https://doi.org/10.1017/jfm.2021.1074, 2022.

Vallero, G., Marchelli, M., and De Biagi, V.: Structural Vulnerability of Power Transmission Line Supports: Development of Fragility Curves for Snow Avalanche Loads, Georisk: Assessment and Management of Risk for Engineered Systems and Geohazards, 0, 1–23, https://doi.org/10.1080/17499518.2026.2616777, 2026.

Védrine, L., Li, X., and Gaume, J.: Detrainment and Braking of Snow Avalanches Interacting with Forests, Natural Hazards and Earth System Sciences, 22, 1015–1028, https://doi.org/10.5194/nhess-22-1015-2022, 2022.

Virtanen, P., Gommers, R., Oliphant, T. E., Haberland, M., Reddy, T., Cournapeau, D., Burovski, E., Peterson, P., Weckesser, W., Bright, J., van der Walt, S. J., Brett, M., Wilson, J., Millman, K. J., Mayorov, N., Nelson, A. R. J., Jones, E., Kern, R., Larson, E., Carey, C. J., Polat, İ., Feng, Y., Moore, E. W., VanderPlas, J., Laxalde, D., Perktold, J., Cimrman, R., Henriksen, I., Quintero, E. A., Harris, C. R., Archibald, A. M., Ribeiro, A. H., Pedregosa, F., van Mulbregt, P., and SciPy 1.0 Contributors: SciPy 1.0: Fundamental Algorithms for Scientific Computing in Python, Nature Methods, 17, 261–272, https://doi.org/10.1038/s41592-019-0686-2, 2020.

Voellmy, A.: Über die Zerstörungskraft von Lawinen; Zur Dynamik der Lawinen, Schweizerische Bauzeitung, 73, https://doi.org/10.5169/SEALS-61891, 1955.

Willibald, C., Löwe, H., Theile, T., Dual, J., and Schneebeli, M.: Angle of Repose Experiments with Snow: Role of Grain Shape and Cohesion, Journal of Glaciology, 66, 658–666, https://doi.org/10.1017/jog.2020.36, 2020.

Wu, Y., Wang, D., Li, P., and Niu, Z.: Experimental Investigation of Dry Granular Flows down an Inclined Channel against a Wall-like Obstacle of Limited Width, Acta Geotechnica, 18, 2141–2154, https://doi.org/10.1007/s11440-022-01714-2, 2023.